International Journal of Thermal Sciences 172 (2022) 107265

Contents lists available at ScienceDirect

International Journal of Thermal Sciences

journal homepage: www.elsevier.com/locate/ijts

On the effect of spatial fractional heat conduction in MHD boundary layer flow using Gr-Fe_3O_4–H_2O hybrid nanofluid

Mehdi Khazayinejad, S.S. Nourazar *

Department of Mechanical Engineering, Amirkabir University of Technology, Tehran, Iran

ARTICLE INFO

Keywords:
Modified Fourier's law
Spatial-fractional diffusion
Hybrid nanofluid
Magnetohydrodynamic
Optimal collocation method

ABSTRACT

In this article, the magnetohydrodynamic boundary layer flow and spatial fractional heat transport of Gr-Fe_3O_4–H_2O hybrid nanofluid on a moving flat plate is investigated. The diffusion terms in the energy equation are modified by incorporating the spatial fractional derivatives using Fourier's law. Moreover, the effect of the joule heating, heat sink/source and viscous dissipation on the energy equation is also taken into account. The optimal collocation method as a new semi-analytical approach is introduced and the effects of physical parameters on the flow and heat transport specifications are obtained and analyzed. It is seen that changing the order of fractional derivatives from 0.92 (fractional diffusion) to 1 (classical diffusion) leads to a growth of the temperature. Furthermore, for the case $\lambda = 0.7$, the Nusselt number of Gr-Fe_3O_4–H_2O augments by 22% when compared to Fe_3O_4–H_2O and by 66% when compared to H_2O. The results of Nusselt number and Skin friction coefficient for Prandtl number of 0.71 are validated by comparing with both the experimental and numerical studies in the existing literature, which confirms that the optimal collocation method can be successfully used to predict the spatial-fractional MHD boundary layer flow.

1. Introduction

The fractional theory has wide applications in the modeling of many physical phenomena and engineering such as signal processing, control theory, rheology, hydrologic cycle, flexible structures, condensed matter physics, electromagnetics, viscoelasticity, optical fibers, image processing, etc [1–3]. In the classical studies of nanofluid flows, the diffusion term is considered by second-order equations and the effect of the space fractional derivatives are not taken into account. Recently, many authors proposed fractional derivatives of diffusion terms in their investigations. Pan et al. [4] presented a numerical solution for stochastic thermal transport that occurs in mixed convection boundary layer flow by considering the modified space fractional derivatives of Fourier's law. Chen et al. [5] numerically studied the effect of space fractional derivatives on MHD boundary layer flow and heat transport of a viscoelastic fluid. Their results indicate that with the augmentation of the fractional parameter, the first-order temperature gradients (Nusselt number) rises; however, opposite behavior appears for wall fractional-order temperature gradients. Tassaddiq [6] examined numerically the MHD mixed convection boundary layer of second grade fluid flow in the vicinity of an inclined periodic plate by considering the Atangana–Baleanu fractional derivatives. Li and Liu [7] discussed the impact of fractional-derivative on viscoelastic fluid through a permeable surface by implicit difference method. The present literature survey illustrates that all attempts to analyze the fractional boundary layer flows are based on the numerical approach.

With the rapid advancement of modern physics, the new techniques for heat transfer augmentation play a vital role in thermal engineering systems. The hybrid nanofluid is a relatively novel branch of heat transfer, which remarkably enhances the heat transfer rate. Recently, several researchers discussed the effect of various combinations of nanoparticles on the hybrid nanofluid flow problems through different geometries [8–11]. Furthermore, Mabood et al. [12] have studied the magnetic field effect on hybrid nanofluid convective flow and their study reveals that the increase of nanoparticle volume fraction leads to an improved heat transfer rate. Tlili et al. [13] have used the shooting scheme to solve a 3-D MHD hybrid nanofluid flow along an irregular dimension sheet in the presence of thermal radiation. Compared with other nanoparticles, the hybrid graphene (*Gr*) and magnetite (Fe_3O_4) have been paying much attention due to their good thermal properties. Askari et al. [14] performed experimental research on the heat transfer of magnetite/graphene/water hybrid nanofluid within a cooling tower. They reported that Nusselt number increases 8.5% and 14.5% for *Gr* –

* Corresponding author.
E-mail address: icp@aut.ac.ir (S.S. Nourazar).

https://doi.org/10.1016/j.ijthermalsci.2021.107265
Received 15 January 2021; Received in revised form 3 August 2021; Accepted 30 August 2021
Available online 11 November 2021

Nomenclature

T	Temperature (K)
X, Y	Cartesian coordinates (m)
U	Velocity in $\overline{X}$ direction $(m\,s^{-1})$
V	Velocity in $\overline{Y}$ direction $(m\,s^{-1})$
q	Heat flux $(W\,m^{-2})$
c_p	Heat capacity $(J\,kg^{-1}\,K^{-1})$
k	Thermal conductivity $(W\,m^{\beta-2}\,K^{-1})$
$Q^{\bullet}$	Internal heat generation $(W\,K^{-1}\,m^{-3})$
B	Magnetic field (T)
Q_s	Heat sink/source parameter
Re	Reynolds number
Ec	Eckert number
Pr	Prandtl number
Ha	Hartmann number
λ	Velocity ratio parameter
W_i	Weight functions
R	Residual function
c	Unknown constants for the trial function
z, g, h	Change of variable
Nu	Nusselt number
C_f	Surface drag coefficient
f'	Non-dimensional velocity

Greek symbols

μ	Viscosity $(kg\,m^{-1}\,s^{-1})$
ρ	Density $(kg\,m^{-3})$
σ	Electrically conductivity $(\Omega^{-1}m^{-1})$
ψ	Stream function $(m^2\,s^{-1})$
η	Similarity variable
φ	Nanoparticles volume fraction
θ	Non-dimensional temperature
Γ	Gamma function
δ	Dirac function
β	Space-fractional parameter

Subscripts

f	Fluid
nf	Nanofluid
hnf	Hybrid nanofluid
np	Nanoparticle
W	Wall
∞	Ambient condition

$Fe_3O_4 - H_2O$ hybrid nanofluid and $Fe_3O_4 - H_2O$ single nanofluid compared to the base fluid at Reynolds number of 4248. Mabood et al. [15] numerically examined the influence of different volume concentrations of $Gr - Fe_3O_4 - H_2O$hybrid nanofluid on a stagnation-point flow with radiative heat. Tao et al. [16] applied a method to prepare a highly stable hybrid nanofluid, where the base fluid is Silicone oil with Fe_3O_4 and Gr nanoparticles. They demonstrate that the temperature rising rate of hybrid nanofluid in solar-thermal energy harvesting improves compared to unitary nanofluids.

The study of magnetohydrodynamic has great importance in engineering and industrial processes. Examples of these processes include electromagnetic pumps, magnetic drug targeting, MHD power generators, plasma studies, and emergency cooling of nuclear reactors. Also, the imposed magnetic field for electrically conducting fluids has attracted considerable attention as a promising approach to control the momentum and heat transport in the boundary layer flow. For example, the usage of the magnetic field is a beneficial approach in the sheet extrusion process to control the transport phenomena during sheet forming operations, resulting in improving product quality. Sardar et al. [17] surveyed the thermal-diffusion and diffusion-thermo effects on a wedge surface in an MHD carreau nanofluid flow using the numerical technique. Makinde et al. [18] carried out a numerical work to investigate the MHD effect on heat and mass transfer of the nanofluid along a stretching convective sheet. Elshehabey et al. [19] considered free convection ferrofluid flow under the influence of MHD in a partial open cavity by dispersing nanoparticles of Fe_3O_4 in water. Their observations revealed that the flow momentum reduces when the magnetic parameter (Hartmann number) increases. Sáchica et al. [20] numerically suggested the mixed convection heat transfer and entropy production analysis of H_2O containing Al_2O_3 nanofluid flow through a channel with double cavity under the presence of a transversal magnetic field. Other studies relevant to the MHD on the boundary layer flow and heat transfer can be seen in Refs. [21–30].

To the best of the authors' knowledge, the problem of spatial fractional heat transfer and boundary layer flow of MHD hybrid nanofluid over a moving plate is studied for the first time. Moreover, the plate is subjected to the mixed impact of joule heating, heat sink/source, and viscous dissipation. Additionally, as a novelty, the optimal collocation method (OCM) as a new semi-analytical method is applied to deal with the infinity boundary conditions as well as space fractional derivatives in MHD boundary layer flow.

2. Mathematical model

We consider a steady laminar boundary layer and heat transport of the hybrid nanofluid flow containing nanoparticles of Gr (φ_{np2}) and Fe_3O_4 (φ_{np1}) dispersed into H_2O along a horizontal moving plate. The plate has velocity U_w and temperature $\overline{T}_w$ whereas the external free stream has velocity U_∞ and temperature T_∞, where $T_w > T_\infty$ as shown in Fig. 1. Here $U_w + U_\infty$ and $\varphi_{np1} + \varphi_{np2}$ represent the composite velocity and volume fraction of nanoparticles, respectively. The hybrid nanofluid flow is considered to be conductive electrically. Then an external magnetic field with intensity $B = B_0X^{-0.5}$ is applied perpendicular to the moving flat plate. The effects of Joule heating and heat sink/source are also considered. Besides, the modified Fourier's law of heat conduction is obtained using spatial fractional derivatives. Then the modified Fourier's law is utilized to analyze the rate of heat transfer [4]:

$$q = -k_{\beta_{hnf}}\nabla^{\beta}T(X,Y) = -k_{\beta_{hnf}}\left(\frac{\partial^{\beta}T}{\partial X^{\beta}}\vec{i} + \frac{\partial^{\beta}T}{\partial Y^{\beta}}\vec{j}\right) \tag{1}$$

where q is the heat flux of the generalized Fourier's law, T is the temperature, X and Y are the coordinates along and normal to the flow direction respectively, $k_{\beta_{hnf}}$ is the generalized thermal conductivity of the hybrid nanofluid, β is the order of gradient where $0 < \beta < 1$ and $\nabla^{\beta}T(X,Y)$ represents the Caputo fractional derivative of function $T(X,Y)$ which is expressed as follows [31]:

$$\nabla^{\beta}T\left(X,Y\right) = {}^{C}D_X^{\beta}\,T\left(X,Y\right)\vec{i} + {}^{C}D_Y^{\beta}\,T\left(X,Y\right)\vec{j}$$
$$= \begin{cases} \dfrac{1}{\Gamma(1-\beta)}\left[\left(\displaystyle\int_0^X \frac{\frac{\partial T(\tau,Y)}{\partial\tau}}{(X-\tau)^{\beta}}d\tau\right)\vec{i} + \left(\displaystyle\int_0^Y \frac{\frac{\partial T(X,\tau)}{\partial\tau}}{(Y-\tau)^{\beta}}d\tau\right)\vec{j}\right], & 0<\beta<1 \\ \left(\dfrac{\partial T}{\partial X}\vec{i} + \dfrac{\partial T}{\partial Y}\vec{j}\right), & \beta = 1 \end{cases} \tag{2}$$

where ${}^{C}D_{\overline{X}}^{\beta}$ and ${}^{C}D_{\overline{Y}}^{\beta}$ are the Caputo's fractional derivative operators

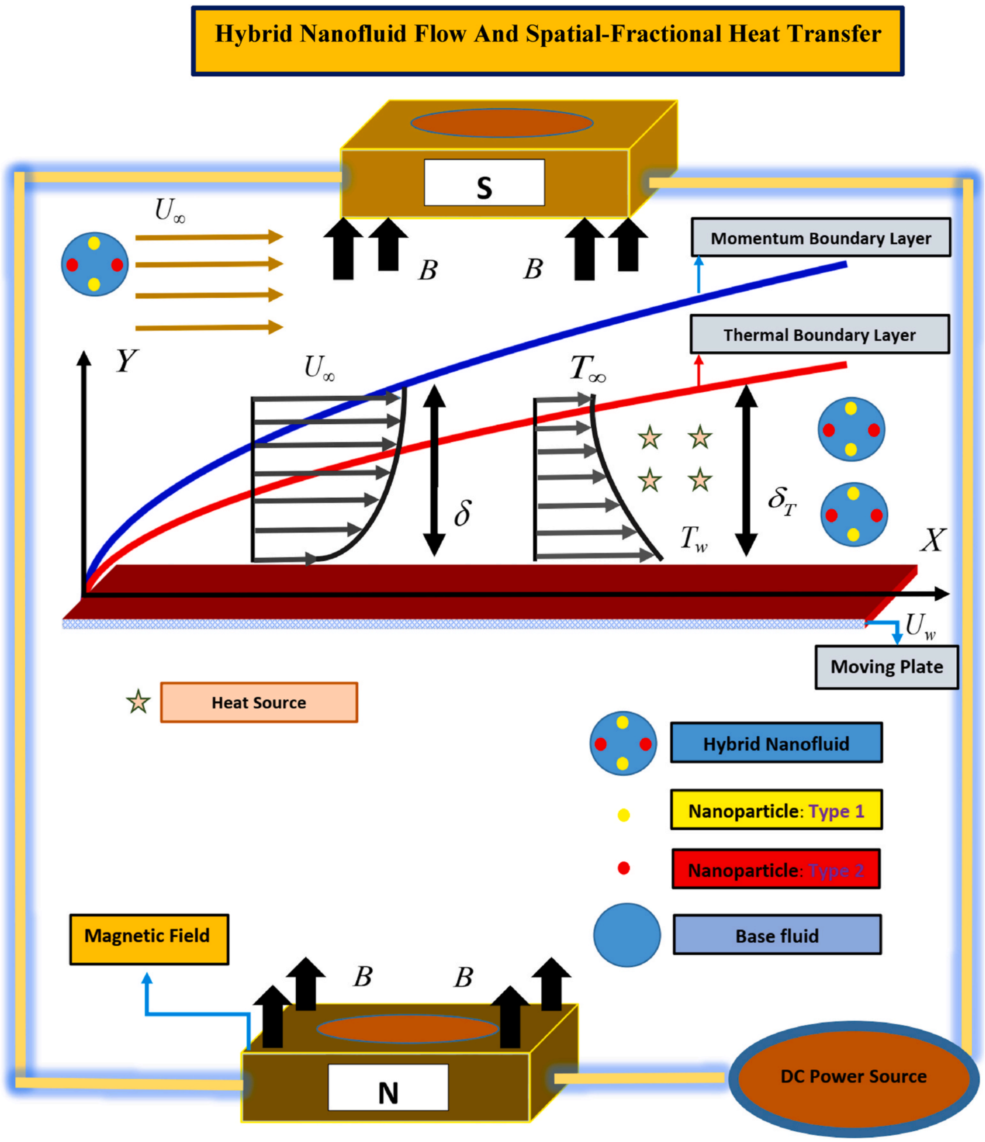

Fig. 1. Geometry of the problem.

and $\Gamma(.)$ is the Gamma function. Regarding the above assumptions, the fundamental equations contain mass, motion, and energy can be expressed as [32–34]:

$$\frac{\partial U}{\partial X}+\frac{\partial V}{\partial Y}=0 \tag{3}$$

$$\rho_{hnf}\left(U\frac{\partial U}{\partial X}+V\frac{\partial U}{\partial Y}\right)=\mu_{hnf}\left(\frac{\partial^2 U}{\partial Y^2}+\frac{\partial^2 U}{\partial Y^2}\right)+\sigma_{hnf}B^2(U_\infty-U) \tag{4}$$

$$\rho_{hnf}\left(U\frac{\partial V}{\partial X}+V\frac{\partial V}{\partial Y}\right)=\mu_{hnf}\left(\frac{\partial^2 V}{\partial X^2}+\frac{\partial^2 V}{\partial Y^2}\right) \tag{5}$$

$$\begin{aligned}(\rho c_p)_{hnf}\left(U\frac{\partial T}{\partial X}+V\frac{\partial T}{\partial Y}\right)&=\frac{k_{\beta_{hnf}}}{\Gamma(1-\beta)}\left[\left(\int_0^X\frac{\frac{\partial^2 T(\tau,\overline{Y})}{\partial\tau^2}}{(X-\tau)^\beta}d\tau\right)+\left(\int_0^Y\frac{\frac{\partial^2 T(X,\tau)}{\partial\tau^2}}{(Y-\tau)^\beta}d\tau\right)\right]\\&+\sigma_{hnf}(U_\infty-U)^2B^2+\underset{\substack{source\\or\\\text{sink}}}{\overset{\bullet}{Q}}(T-T_\infty)+\mu_{hnf}\left[2\left(\frac{\partial U}{\partial X}\right)^2+2\left(\frac{\partial V}{\partial Y}\right)^2+\left(\frac{\partial U}{\partial Y}+\frac{\partial V}{\partial X}\right)^2\right]\end{aligned} \tag{6}$$

in which (U,V) represent the components of velocity in the (X,Y) directions, β is the fractional parameter, T is the temperature inside the boundary layer and $Q^\bullet=Q_0X^{-1}$ is the internal heat generation which $Q^\bullet<0$ and $Q^\bullet>0$ are heat sink and heat source respectively. The thermophysical properties of hybrid nanofluid, ρ_{hnf}, μ_{hnf}, σ_{hnf}, $c_{p_{hnf}}$ and k_{hnf} are the density, dynamic viscosity, electrical conductivity, heat capacity, and generalized thermal conductivity of hybrid nanofluid respectively [35,36]:

$$\rho_{hnf}=(1-\varphi_{np1}-\varphi_{np2})\rho_f+\varphi_{np1}\rho_{np1}+\varphi_{np2}\rho_{np2} \tag{7}$$

$$\mu_{hnf}=\frac{\mu_f}{(1-\varphi_{np1}-\varphi_{np2})^{2.5}} \tag{8}$$

$$\sigma_{hnf}=\sigma_f+\frac{3\sigma_f(\varphi_{np1}+\varphi_{np2})(\varphi_1\sigma_{np1}+\varphi_2\sigma_{np1}-\sigma_f(\varphi_{np1}+\varphi_{np2}))}{\begin{pmatrix}\varphi_{np1}\sigma_{np1}+\varphi_{np2}\sigma_{np2}\\+2(\varphi_{np1}+\varphi_{np2})\sigma_f\end{pmatrix}-(\varphi_{np1}+\varphi_{np2})\begin{pmatrix}(\varphi_{np1}\sigma_{np1}+\varphi_{np2}\sigma_{np2})\\-(\varphi_{np1}+\varphi_{np2})\sigma_f\end{pmatrix}} \tag{9}$$

$$(\rho c_p)_{hnf}=(1-\varphi_{np1}-\varphi_{np2})(\rho c_p)_f+\varphi_{np1}(\rho c_p)_{np1}+\varphi_{np2}(\rho c_p)_{np2} \tag{10}$$

$$k_{\beta_{hnf}}=k_f\frac{\varphi_{np1}k_{np1}+\varphi_{np2}k_{np2}+2(\varphi_{np1}+\varphi_{np2})(\varphi_{np1}k_{np1}+\varphi_{np2}k_{np2})-2(\varphi_{np1}+\varphi_{np2})^2k_f}{\varphi_{np1}k_{np1}+\varphi_{np2}k_{np2}+2(\varphi_{np1}+\varphi_{np2})k_f-(\varphi_{np1}+\varphi_{np2})(\varphi_{np1}k_{np1}+\varphi_{np2}k_{np2})+(\varphi_{np1}+\varphi_{np2})^2k_f} \tag{11}$$

in which φ_{np1} and φ_{np2} stand for the magnetite nanoparticles and graphene volume fractions, respectively. Table 1 displays the thermophysical properties of base fluid and nanoparticles [37,38]. The Relevant boundary conditions are:

$$U=U_w,\quad V=0,\quad T=T_w\quad at\quad Y=0 \tag{12}$$

$$U=U_\infty,\quad T=T_\infty\quad at\quad Y=\infty \tag{13}$$

The similarity transformation variables are defined as [32]:

$$\eta=\frac{Y}{\sqrt{\frac{\nu_f X}{U_w+U_\infty}}},\quad f=\frac{-\psi(X,Y)}{\sqrt{\nu_f X(U_w+U_\infty)}},\quad \theta=\frac{T-T_\infty}{T_w-T_\infty} \tag{14}$$

Here, f is the non-dimensional stream function dependent on the variable η, ψ is the stream function and θ is the non-dimensional temperature. Moreover, the stream function ψ is defined to satisfy the continuity equation (Eq. (4)) as:

$$U=\frac{-\partial\psi}{\partial\overline{Y}},\quad V=\frac{\partial\psi}{\partial\overline{X}} \tag{15}$$

According to Eqs. (14) and (15) we can deduce:

$$U=(U_w+U_\infty)f'(\eta),\quad V=\sqrt{\frac{\nu_f(U_w+U_\infty)}{4\overline{X}}}(\eta f'(\eta)-f(\eta)) \tag{16}$$

where prime signifies derivatives with respect to η. Under the above similarity transformations, boundary layer approximations and using the Caputo's fractional derivative model, Eqs. (4)–(6) can be re-arranged as follows:

$$f''(\eta)+\frac{1}{2}\frac{\rho_{hnf}}{\rho_f}\frac{\mu_f}{\mu_{hnf}}f(\eta)f''(\eta)+Ha\frac{\sigma_{hnf}}{\sigma_f}\frac{\mu_f}{\mu_{hnf}}(1-\lambda-f'(\eta))=0, U_\infty \tag{17}$$

$$\frac{k_{\beta_{hnf}}}{k_f}\left(\frac{\nu_f X}{(U_w+U_\infty)}\right)^{\frac{1-\beta}{2}}\frac{1}{\Gamma(1-\beta)}\left(\int_0^\eta\frac{\frac{d^2\theta(\tau)}{d\tau^2}}{(\eta-\tau)^\beta}d\tau\right)+\frac{Pr}{2}\frac{(\rho c_p)_{hnf}}{(\rho c_p)_f}f(\eta)\theta'(\eta)$$
$$+Ha\,Pr\,Ec\frac{\sigma_{hnf}}{\sigma_f}(1-\lambda-f'(\eta))^2+Pr\,Q_s\,\theta(\eta)+\frac{\mu_{hnf}}{\mu_f}Pr\,Ec\,f''^2(\eta)=0 \tag{18}$$

The boundary conditions for equations (17) and (18) become:

$$f(0)=0,\quad f'(0)=\lambda,\quad f'(\infty)=1-\lambda,$$
$$\theta(0)=1,\quad \theta(\infty)=0 \tag{19}$$

In Eqs. (17) and (18) the dimensionless parameters (λ), (Ha), (Ec), (Pr) and (Q_s).are the velocity ratio parameter, Hartmann number, Eckert number, Prandtl number, and Heat sink/source parameter respectively. The dimensionless parameters are defined as follows:

$$\lambda=\frac{U_w}{(U_w+U_\infty)},\quad Ha=\frac{\sigma_f B_0^2}{\rho_f(U_w+U_\infty)},\quad Ec=\frac{(U_w+U_\infty)^2}{c_{p_f}(T_w-T_\infty)},\quad Pr=\frac{\nu_f(\rho c_p)_f}{k_f},$$
$$Q_s=\frac{Q_0}{(\rho c_p)_f(U_w+U_\infty)} \tag{20}$$

The surface drag coefficient C_f and local Nusselt number Nu may be obtained by:

$$C_f=\frac{\tau_w}{\frac{1}{2}\rho_f(U_w+U_\infty)^2},\quad Nu=\frac{Xq_w}{k_f(T_w-T_\infty)} \tag{21}$$

Here τ_w and q_w denote the shear stress and heat flux on the plate-fluid interface, respectively, can be defined by:

$$\tau_w=\mu_{hnf}\left(\frac{\partial U}{\partial Y}\right)_{\overline{Y}=0},\quad q_w=-k_{\beta_{hnf}}\left(\frac{\partial^\beta T}{\partial Y^\beta}\right)_{\overline{Y}=0} \tag{22}$$

Therefore, Eq. (21) can be simplified as:

$$C_f\sqrt{Re}=\frac{2}{(1-\varphi_{np1}-\varphi_{np2})^{2.5}}f''(0)=C_{f_r} \tag{23}$$

$$\frac{Nu}{\sqrt{Re}}=-\frac{k_{\beta_{hnf}}}{k_f}\left(\frac{\upsilon_f X}{(U_w+U_\infty)}\right)^{\frac{1-\beta}{2}}\left(\frac{\partial^\beta\theta}{\partial\eta^\beta}\right)_{\eta=0}=Nu_r \tag{24}$$

in which $Re=\frac{(U_w+U_\infty)X}{\nu_f}$ represents the Reynolds number.

When $\beta=1$, Eq. (25) may be reduced to Ref. [39]:

$$Nu=0.332\,Pr^{1/3}Re^{1/2},\quad 0.6<Pr \tag{25}$$

3. The optimal collocation method and problem solution

In what follows, the optimal collocation method (OCM) is applied to achieve a semi-analytical solution of Eqs. (17) and (18). This method is suggested via Khazayinejad et al. [34,40] and Nourazar et al. [41] in their articles for the solution of boundary layer equations with semi-infinite domain to optimize the collocation method (CM) [42]. The key points of the OCM are to use the asymptotic boundary conditions and transformation of the physical domain to a computational domain. The semi-infinite domain, $0\le\eta<\infty$, may be converted into the interval $0\le\eta\le\eta_\infty$ which η_∞ depends on the physical parameters. Moreover, by making the change of variable $z=\eta/\eta_\infty$, $g(z)=f(\eta)/\eta_\infty$and $h(z)=\theta(\eta)/\eta_\infty$, the interval $0\le\eta\le\eta_\infty$ can be replaced by $0\le z\le1$, therefore, Eqs. (17) and (18) are rewritten as:

$$\frac{1}{\eta_\infty^2}g'''(z)+\frac{1}{2}\frac{\rho_{hnf}}{\rho_f}\frac{\mu_f}{\mu_{hnf}}g(z)g''(z)+Ha\frac{\sigma_{hnf}}{\sigma_f}\frac{\mu_f}{\mu_{hnf}}(1-\lambda-g'(z))=0 \tag{26}$$

$$\frac{1}{\eta_\infty^\beta}\frac{k_{\beta_{hnf}}}{k_f}\left(\frac{\nu_f X}{(U_w+U_\infty)}\right)^{\frac{1-\beta}{2}}\frac{1}{\Gamma(1-\beta)}\left(\int_0^z\frac{\frac{d^2h(\tau)}{d\tau^2}}{(\eta-\tau)^\beta}d\tau\right)+\eta_\infty\frac{Pr}{2}\frac{(\rho c_p)_{hnf}}{(\rho c_p)_f}g(z)h'(z)$$
$$+Ha\,Pr\,Ec\frac{\sigma_{hnf}}{\sigma_f}(1-\lambda-g'(z))^2+\eta_\infty Pr\,Q_s\,h(z)+\frac{1}{\eta_\infty^2}\frac{\mu_{hnf}}{\mu_f}Pr\,Ec\,f''^2(z)=0 \tag{27}$$

where the "′" signifies the derivatives on the z ∈ [0,1]. The following new boundary conditions are obtained using the change of variable as:

Table 1
Thermophysical properties of base fluid and nanoparticles [37,38].

Properties	ρ ($kg\,m^{-3}$)	c_p ($J\,kg^{-1}\,K^{-1}$)	k ($W\,m^{-1}\,K^{-1}$)	σ($\Omega^{-1}m^{-1}$)
Water	997.1	4179	0.613	0.05
Magnetite	5200	670	6	25,000
Graphene	2250	2100	2500	10^7

$$
\begin{aligned}
&g(0)=0, \quad g^{'}(0)=\lambda, \quad g^{'}(1)=1-\lambda, \quad g''(1)=0 \\
&h(0)=\frac{1}{\eta_\infty}, \quad h(1)=0, \quad h^{'}(1)=0
\end{aligned}
\tag{28}
$$

where $g''(1)=0$ and $h^{'}(1)=0$designate the boundary conditions for shear stress and rate of heat transfer in the computational domain at infinity. This is the novel aspect of contribution in the present analysis where the boundary condition at infinity is taken into account. By having considered the boundary conditions at infinity one may expect more accurate results in the asymptotic area of the nanofluid boundary layer flow. Suitable trial functions including unknown coefficients "c" are considered as follows [34,41,43,44]:

$$
g(z)=\frac{1}{\eta_\infty}\left(c_0+\sum_{i=1}^{k} c_i\, z^i\right)=\frac{1}{\eta_\infty}\left(c_0+c_1\, z+c_2\, z^2+\ldots+c_k\, z^k\right) \tag{29}
$$

$$
h(z)=\frac{1}{\eta_\infty}\left(c_{k+1}+\sum_{i=1}^{m} c_{i+k+1}\, z^{\beta i}\right)=\frac{1}{\eta_\infty}\left(c_{k+1}+c_{k+2}\, z^{\beta}+c_{k+3}\, z^{2\beta}+\ldots+c_{m+k+1}\, z^{m\beta}\right) \tag{30}
$$

The precision of the trial functions may be enhanced by considering more terms in sequences of Eqs. (29) and (30). In the OCM, unlike the CM, the number of required weight functions is not essential to be exactly equivalent to the number of unfamiliar constants. In this method the number of weight functions W_i can be written as:

$$
n_{W_i}=n_{c_i}+1-n_b-n_e \tag{31}
$$

In this equation, n_{W_i}, n_{c_i}, n_b and n_a are the number of weight functions, the number of unknown constants, the number of boundary conditions and the number of asymptotic boundary conditions, respectively. To satisfy the boundary conditions of Eq. (28), one may proceed as follows:

$$
z=0 \;\Rightarrow\; g=0 \;\Rightarrow\; c_0=0 \tag{32}
$$

$$
z=0 \;\Rightarrow\; g^{'}=\lambda \;\Rightarrow\; c_1=\lambda\eta_\infty \tag{33}
$$

$$
z=1 \;\Rightarrow\; g^{'}=1-\lambda \;\Rightarrow\; \frac{1}{\eta_\infty}(c_1+2c_2+\ldots+kc_k)=1-\lambda \tag{34}
$$

$$
z=0 \;\Rightarrow\; h=\frac{1}{\eta_\infty} \;\Rightarrow\; c_{k+1}=1 \tag{35}
$$

$$
z=1 \;\Rightarrow\; h=0 \;\Rightarrow\; c_{k+1}+c_{k+2}+c_{k+3}+\ldots+c_{m+k+1}=0 \tag{36}
$$

$$
z=1 \;\Rightarrow\; g''=0 \;\Rightarrow\; 2c_2+6c_3+\ldots+k(k-1)c_k=0 \tag{37}
$$

$$
z=1 \;\Rightarrow\; h^{'}=0 \;\Rightarrow\; c_{k+2}+2c_{k+3}+\ldots+mc_{m+k+1}=0 \tag{38}
$$

Now by putting g and h in Eqs. (26) and (27), the residual functions can be obtained:

$$
\begin{aligned}
R_g(c_0,c_1,\ldots,c_k)={}&\frac{1}{\eta_\infty^3}\frac{d^3}{dz^3}\left(c_0+\sum_{i=1}^{k} c_i\, z^i\right)+\frac{1}{2\eta_\infty^2}\frac{\rho_{hnf}}{\rho_f}\frac{\mu_f}{\mu_{hnf}}\left(c_0+\sum_{i=1}^{k} c_i\, z^i\right) \\
&\frac{d^2}{dz^2}\left(c_0+\sum_{i=1}^{k} c_i\, z^i\right)+Ha\frac{\sigma_{hnf}}{\sigma_f}\frac{\mu_f}{\mu_{hnf}}\left(1-\lambda-\frac{1}{\eta_\infty}\frac{d}{dz}\left(c_0+\sum_{i=1}^{k} c_i\, z^i\right)\right)
\end{aligned}
\tag{39}
$$

$$
\begin{aligned}
R_h(c_0,c_1,\ldots,c_{m+k+1})={}&\frac{k_{\beta_{hnf}}}{\eta_\infty^{\beta+1}\, k_f\, \Gamma(1-\beta)}\left(\frac{\nu_f X}{(U_w+U_\infty)}\right)^{\frac{1-\beta}{2}} \\
&\left(\int_0^z \frac{\frac{d^2}{d\tau^2}\left(c_{k+1}+\sum_{i=1}^{m} c_{i+k+1}\, \tau^{\beta i}\right)}{(z-\tau)^{\beta}}d\tau\right)+\frac{1}{\eta_\infty}\frac{Pr}{2}\frac{(\rho c_p)_{hnf}}{(\rho c_p)_f}\left(c_0+\sum_{i=1}^{k} c_i\, z^i\right) \\
&\frac{d}{dz}\left(c_{k+1}+\sum_{i=1}^{m} c_{i+k+1}\, z^{\beta i}\right)+Ha\, Pr\, Ec\,\frac{\sigma_{hnf}}{\sigma_f}\left(1-\lambda-\frac{1}{\eta_\infty}\frac{d}{dz}\left(c_0+\sum_{i=1}^{k} c_i\, z^i\right)\right)^2 \\
&+Pr\, Q_s\left(c_{k+1}+\sum_{i=1}^{m} c_{i+k+1}\, z^{\beta i}\right)+\frac{1}{\eta_\infty^3}\frac{\mu_{hnf}}{\mu_f}Pr\, Ec\left(\frac{d^2}{dz^2}\left(c_0+\sum_{i=1}^{k} c_i\, z^i\right)\right)^2
\end{aligned}
\tag{40}
$$

Further, the basis of the OCM is to oblige the residuals tend to zero as:

$$
\int_z R(z)\, W_i(z)=0 \quad ,i=1,2,\ldots,n \tag{41}
$$

Here, $W_i(z)$is the weight function that is selected as:

$$
W_i(z)=\delta(z-z_i) \tag{42}
$$

where $\delta(z-z_i)$ is the Dirac delta function. After utilizing weight functions (Eq. (42)) into Eq. (41),

$$
\begin{aligned}
&R_g\left(\frac{1}{k-1}\right)=0 \quad , \quad R_g\left(\frac{2}{k-1}\right)=0 \quad , \quad R_g\left(\frac{3}{k-1}\right) \\
&\qquad =0 \quad ,\ldots, \quad R_g\left(\frac{k-2}{k-1}\right)=0
\end{aligned}
\tag{43}
$$

$$
\begin{aligned}
&R_h\left(\frac{1}{m-1}\right)=0 \quad , \quad R_h\left(\frac{2}{m-1}\right)=0 \quad , \quad R_h\left(\frac{3}{m-1}\right) \\
&\qquad =0 \quad ,\ldots, \quad R_h\left(\frac{m-2}{m-1}\right)=0
\end{aligned}
\tag{44}
$$

Thus, we have a set of $k+m+3$ equations including Eqs. (32) - (38) and Eqs. (43) - (44). By solving the corresponding equations, the unknown coefficients c_i and η_∞ can be computed. These values are substituted into Eqs (29) and (30) to calculate the velocity and temperature profiles. For a special of $Gr-Fe_3O_4-H_2O$ hybrid nanofluid with $Ha=2$, $Q_s=0.1$, $Pr=6.2$, $Ec=0.2$, $\lambda=0.7$, $X=1$, $\varphi_{np1}=0.02$, $\varphi_{np2}=0.02$, $\beta=0.98$, $k=7$and $m=8$, the approximate solution is:

$$
f(\eta)=0.7\,\eta-0.293734596\,\eta^2+0.133531404\,\eta^3+\ldots+0.000051312\,\eta^7 \tag{45}
$$

$$
\theta(\eta)=1-0.3394714396\,\eta^{\frac{49}{50}}-1.310020044\,\eta^{\frac{49}{25}}+\ldots+0.000043923\,\eta^{\frac{196}{25}} \tag{46}
$$

Also, in an analogous procedure, the solutions of the problem for other values of parameters are examined in the results section.

4. Validation of the solution

To prove the validity of the OCM, the obtained Skin friction coefficient, Nusselt number, dimensionless stream functions, and velocity profiles are compared with those available from the literature ([45–55]).

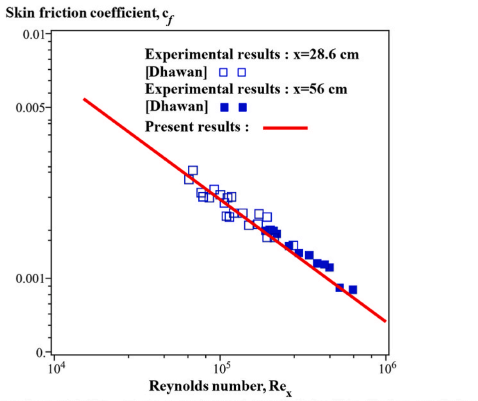

a. Comparison of OCM with the experimental data [45] for Skin friction coefficient

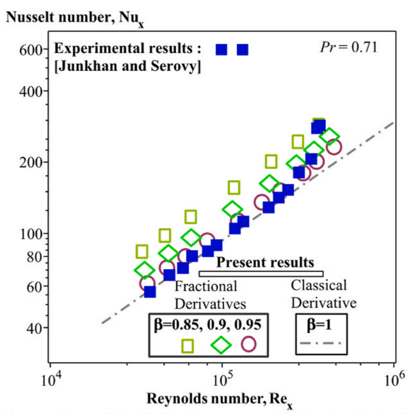

b. Comparison of the experimental data [46] with present results (classical derivative results and fractional derivatives results) for Nusselt number

Fig. 2. a. Comparison of OCM with the experimental data [45] for Skin friction coefficient. Fig. 2b. Comparison of the experimental data [46] with present results (classical derivative results and fractional derivatives results) for Nusselt number.

4.1. Experimental validation

Fig. 2a compares present results with wind tunnel measurements for Skin friction coefficient by Dhawan [45] for the limiting case $Ha = 0$, $\varphi_{np} = 0$, $Pr = 0.71$. Also, the Reynolds number ranges from 10^4 to 10^6. The agreement of the OCM with the experimental data for the skin friction coefficient is excellent. Also, Fig. 2b is used to check the applicability of the present fractional calculus model in capturing the experimental Nusselt number (obtained from wind tunnel measurements) by Junkhan and Serovy [46]. Here, case $\beta = 1$ corresponds to the classical model while $0 < \beta < 1$ ($\beta = 0.85$, $\beta = 0.9$, and $\beta = 0.95$) is for the fractional calculus model. It is noteworthy that the fractional order $\beta = 0.95$ is provided a better fit for the experimental data in comparison with the classical model (especially for larger Reynolds numbers) and other values of the fractional orders. Thus, the spatial fractional heat transport may be used as a new candidate for modeling heat transfer of fluids flow.

4.2. Theoretical validation

In order to validate the outcome of the present investigation with theory results, we make a comparison with the results of [47,48] for dimensionless stream functions and velocity profiles. These comparisons are shown in Fig. 3a and b. An excellent match is seen between the results in both cases. Also, Fig. 4a and b shows the comparison of our results with the numerical results obtained by the Runge–Kutta method for $U_\infty > U_w$ and $U_w > U_\infty$, respectively. It is obvious from the figures that the OCM agrees well with the Runge–Kutta method. Another code validation test is performed in Tables 2 and 3 to compare the present results with the previously published works by Refs. [48–55] for reduced Skin friction coefficient and reduced Nusselt number. A good agreement may be observed from the comparison of the results.

5. Results and discussions

This section presents the behavior of dimensionless velocity $f'(\eta)$, temperature $\theta(\eta)$, reduced skin friction coefficient C_{f_r} and reduced Nusselt number Nu_r for various flow parameters in graphical and tabular forms. For the intention of discussing the results, the default values for variables are: $Ha = 2$, $Q_s = 0.1$, $Pr = 6.2$, $\lambda = 0.4$, $X = 1$, $\varphi_{np1} = 0.02$, $\varphi_{np2} = 0.02$ and $\beta = 0.98$. Further, the results of investigation on the velocity and temperature profiles are illustrated for two cases of $\lambda = 0.4$ and $\lambda = 0.7$. It is worth mentioning that $0 < \lambda < 0.5$ pertains to $U_w > U_\infty$ (the moving surface velocity is greater than that of the free stream) while $0.5 < \lambda < 1$ connects with $U_\infty > U_w$ (the velocity of the free stream is larger than that of the plate).

Figs. 5–7 show the velocity distribution (Fig. 5a and b), shear stress (Fig. 6a and b), and temperature (Fig. 7a and b) of the inner region of the boundary layer flow for several values of velocity ratio parameter λ. It is observed that for $0 < \lambda < 0.5$, the values of the absolute magnitude of the shear stress decrease with the increase of λ, whereas for $0.5 < \lambda < 1$

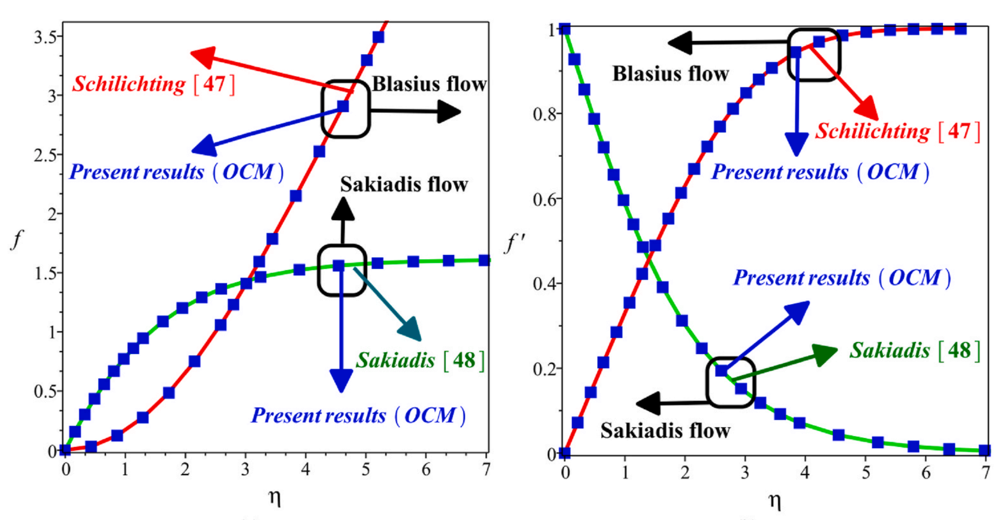

Fig. 3. Comparison of OCM with the available references [47,48] for (a) stream function (b) velocity field.

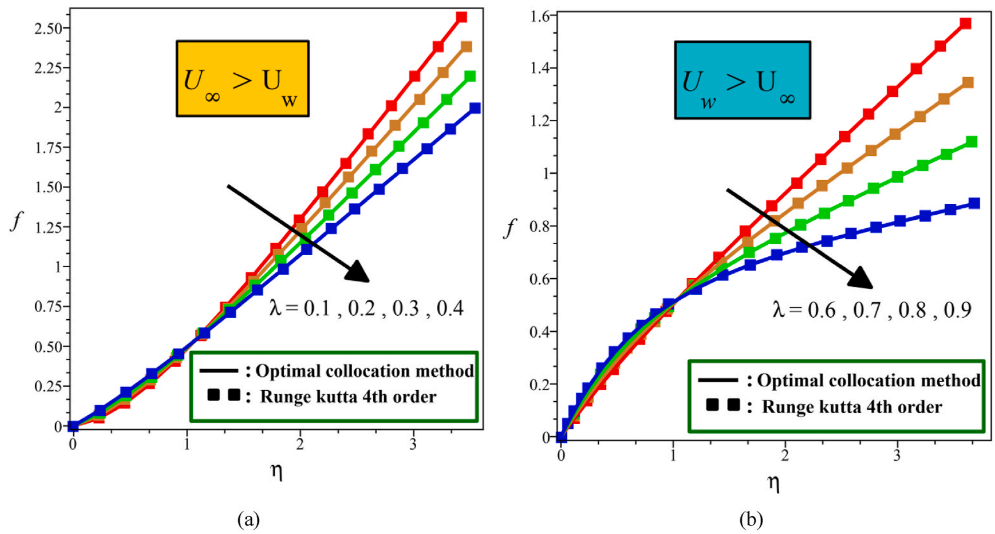

Fig. 4. Comparison of OCM and numerical results for various values of λ(a) $\overline{U}_\infty > \overline{U}_w$(b) $\overline{U}_w > \overline{U}_\infty$

Table 2
Comparison of between the present study and previous studies for reduced skin friction coefficient number ($f''(0)$) when $\phi = Ec = Ha = Q_s = 0, \beta = 1$ and.$Pr = 0.7$

$f''(0)$ Blasius flow ($\lambda = 0$)			$-f''(0)$ Sakiadis flow ($\lambda = 1$)		
Blasius [49]	Schetz [50]	Present study	Sakiadis [48]	Ishak et al. [51]	Present study
0.3321	0.332	0.3321	0.44375	0.4438	0.44371

Table 3
Comparison of between the present study and previous studies for reduced Nusselt number ($\theta'(0)$) when $\phi = Ec = Ha = Q_s = 0$, $\beta = 1$and.$Pr = 0.7$

$-\theta'(0)$ Blasius flow ($\lambda = 0$)			$-\theta'(0)$ Sakiadis flow ($\lambda = 1$)		
Pohlhausen [52]	Oosthuizen [53]	Present study	Chen [54]	Bachok [55]	Present study
0.295	0.2930	0.2929	0.3492	0.34925	0.34929

an opposite trend is seen. It means that in the neighborhood of the plate the velocity grows for all values of λ. But, in both cases, the velocity decreases after a crossover point. Because at this point, the velocity inside the boundary layer attains the outer flow velocity. Also, it is noticed that as λ increases, the thickness of the thermal boundary layer and temperature profile decrease for $U_\infty > U_w$, and they increase when $U_w > U_\infty$.

Fig. 8a and b shows the efficacy of the heat sink/source parameter Q_s on the temperature profile. The heat sink/source parameter is positive ($Q_s > 0$)for heat generation and negative ($Q_s < 0$) for heat absorption, where for $Q_s = 0$ there is no heat generation/absorption. The positive and negative Q_s have different influences on the temperature distribution. As it can be illustrated in Fig. 8a, for $Q_s > 0$ the temperature profile rises with increasing Q_s but for $Q_s < 0$ it starts decreasing as shown in Fig. 8b.

Fig. 9a and b elucidate the velocity field by increasing the Hartmann number Ha. Basically, the Hartmann number is the ratio of magnetic forces to viscous forces. The value of $Ha = 0$ signifies the hydrodynamic flow while $Ha > 0$corresponds to the magneto-hydrodynamic flow (MHD). Physically, applying a magnetic field perpendicular to the plate creates a body force called the Lorentz force, producing resistance in hybrid nanofluid flow. Thus, for $U_w > U_\infty$, the fluid flow velocity

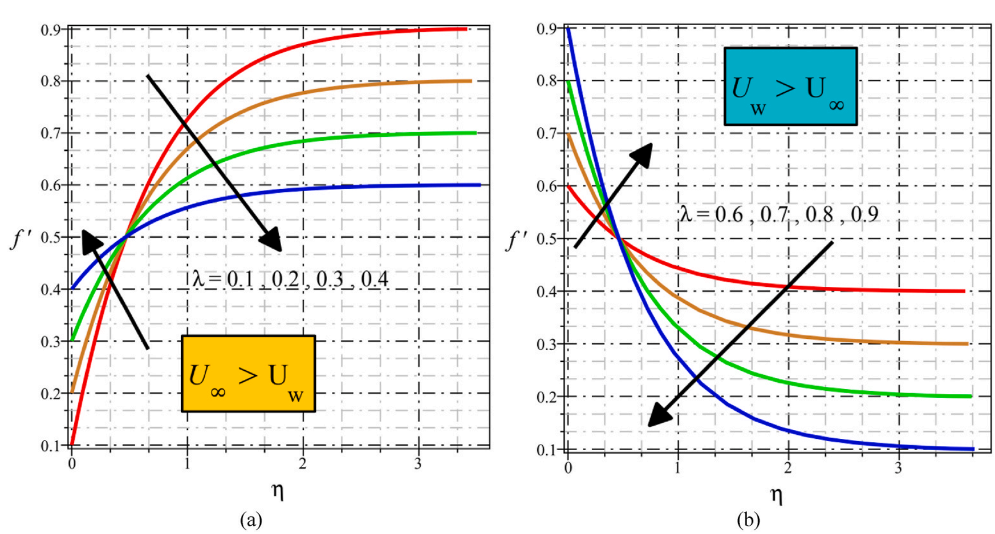

Fig. 5. Velocity profiles for various values of $\lambda$when (a) $\overline{U}_\infty > \overline{U}_w$(b) $\overline{U}_w > \overline{U}_\infty$

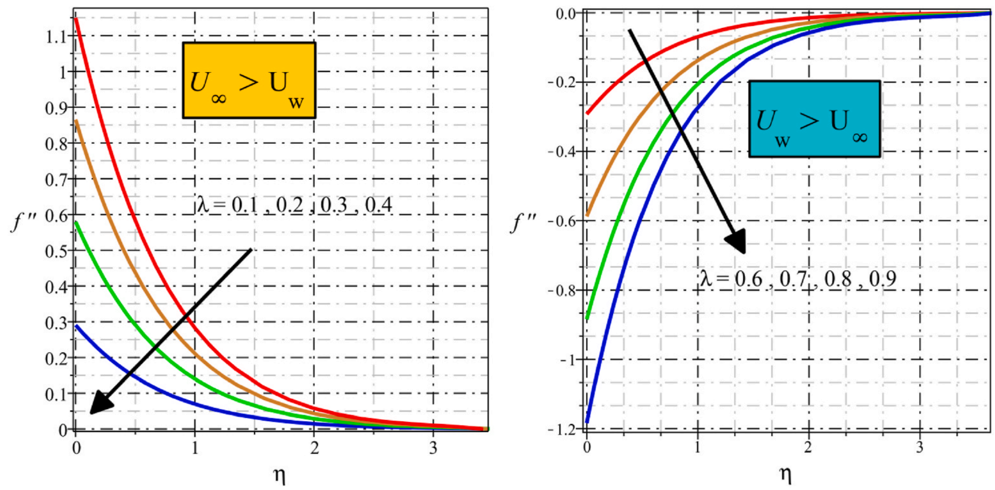

(a) (b)

Fig. 6. Shear stress for various values of $\lambda$when (a) $\overline{U}_\infty > \overline{U}_w$(b) $\overline{U}_w > \overline{U}_\infty$

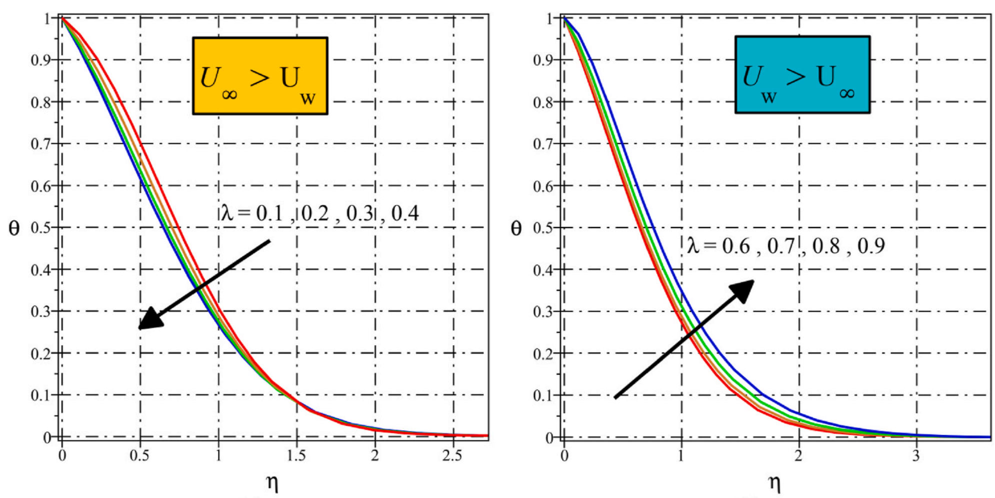

(a) (b)

Fig. 7. Temperature profiles for various values of $\lambda$when (a) $\overline{U}_\infty > \overline{U}_w$(b) $\overline{U}_w > \overline{U}_\infty$

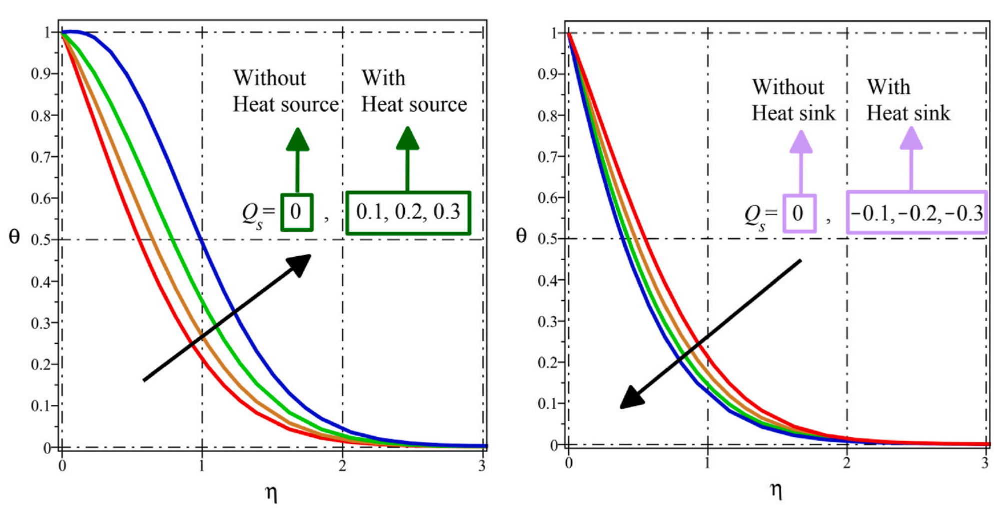

(a) (b)

Fig. 8. Temperature profiles for various values of $Q_s$when (a) $Q_s > 0$(b) $Q_s < 0$

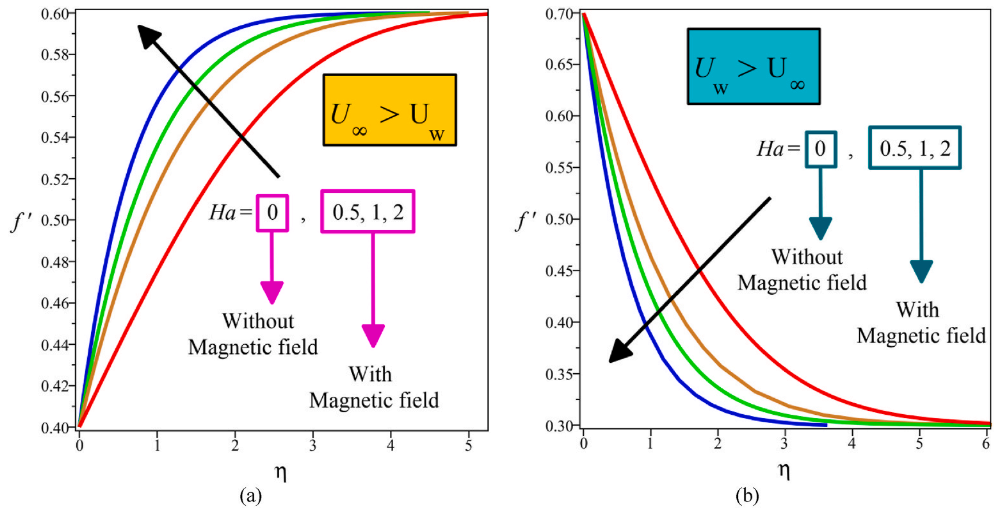

Fig. 9. Velocity profiles for various values of $Ha$when (a) $\overline{U}_\infty > \overline{U}_w$(b) $\overline{U}_w > \overline{U}_\infty$

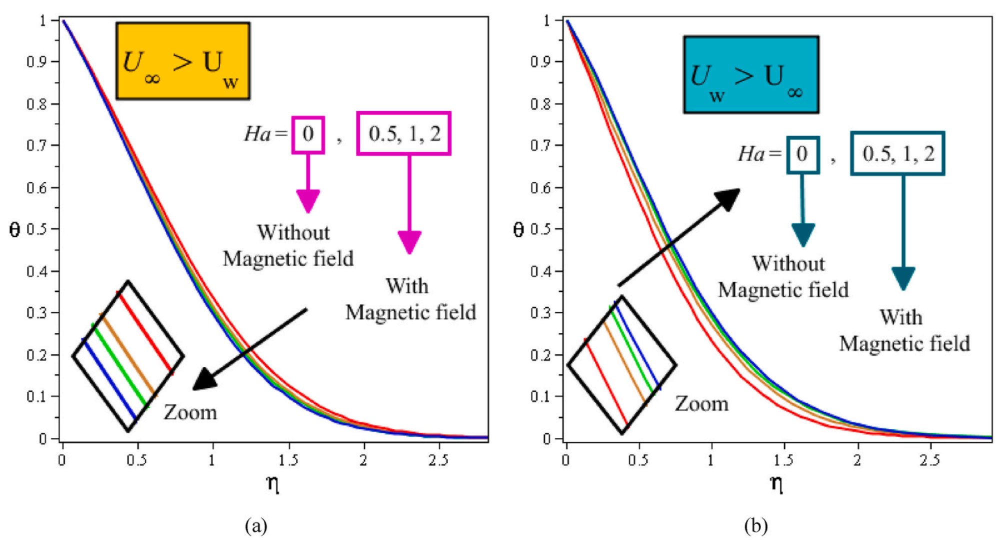

Fig. 10. Temperature profiles for various values of $Ha$when (a) $\overline{U}_\infty > \overline{U}_w$(b) $\overline{U}_w > \overline{U}_\infty$

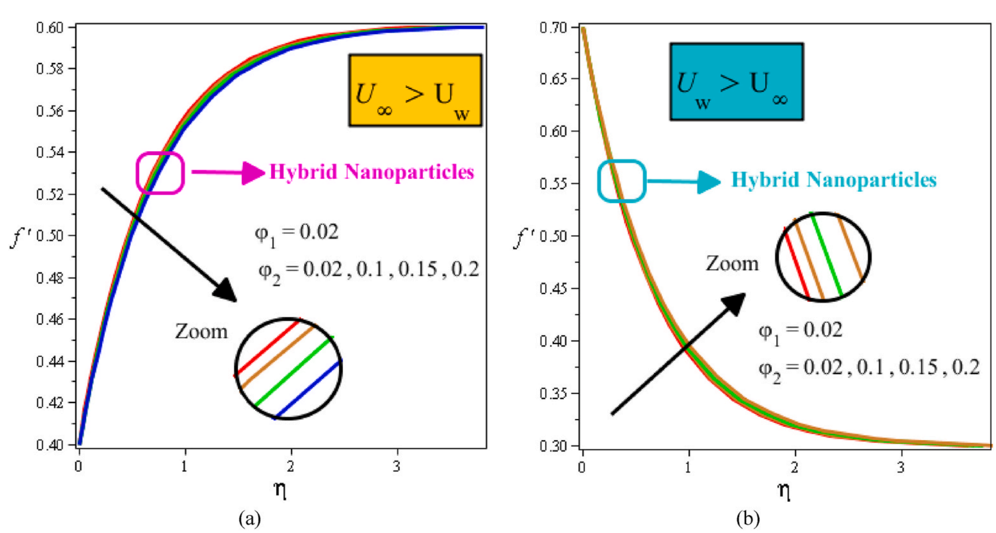

Fig. 11. Velocity profiles for various values of $\varphi_{np2}$when (a) $\overline{U}_\infty > \overline{U}_w$(b) $\overline{U}_w > \overline{U}_\infty$

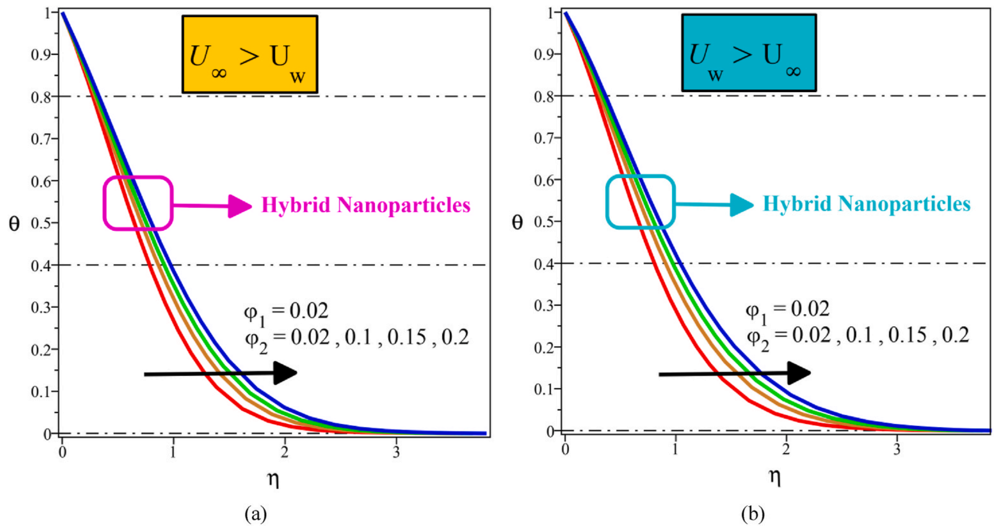

Fig. 12. Temperature profiles for various values of $\varphi_{np2}$when (a) $\overline{U}_{\infty} > \overline{U}_{w}$(b) $\overline{U}_{w} > \overline{U}_{\infty}$

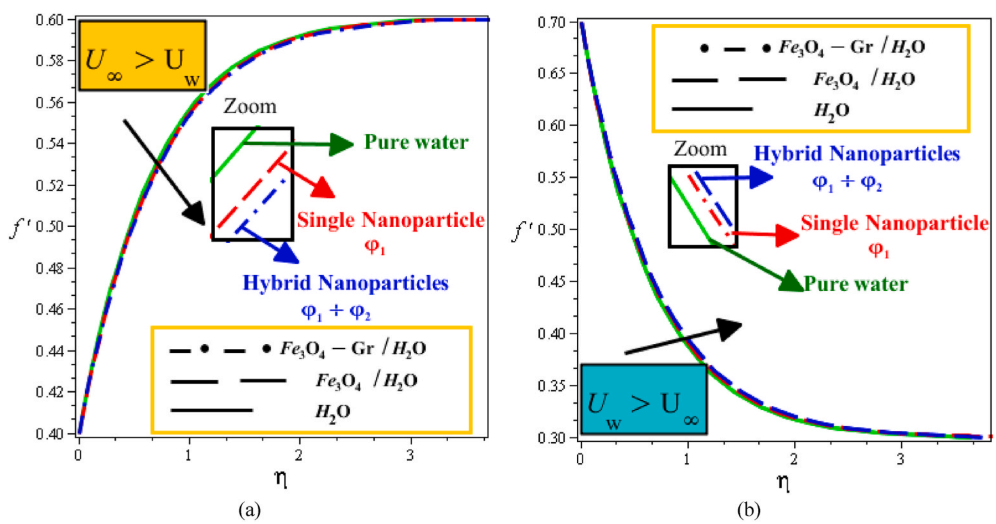

Fig. 13. Velocity profiles for different fluids when (a) $\overline{U}_{\infty} > \overline{U}_{w}$(b) $\overline{U}_{w} > \overline{U}_{\infty}$

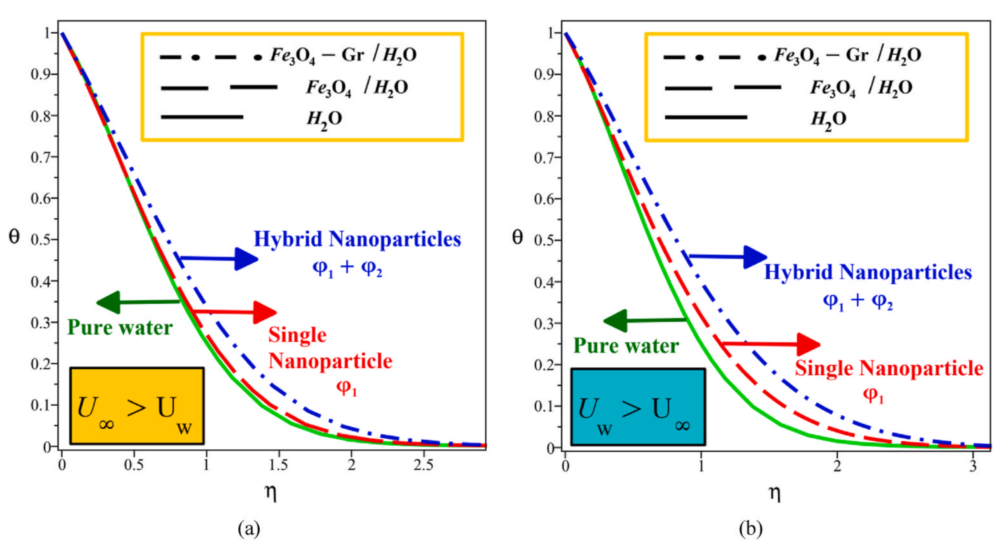

Fig. 14. Temperature profiles for different fluids when (a) $\overline{U}_{\infty} > \overline{U}_{w}$(b) $\overline{U}_{w} > \overline{U}_{\infty}$

reduces. However, for $U_\infty > U_w$, the velocity rises due to the increase of the favorable pressure gradient. The role of Ha on temperature is portrayed in Fig. 10a and b. It is noticed that enhancement in Ha boosts temperature distribution and associated boundary layer thickness for both $U_\infty > U_w$ and $U_w > U_\infty$. As a result, MHD can control the fluid flow's temperature and velocity, which is helpful in many industrial applications such as magnetohydrodynamic, power generation, and electromagnetic coating of wires and metal.

The velocity profile verses the nanoparticle volume fraction φ is depicted in Fig. 11a and b, respectively. In these figures, the volumetric fraction of Fe_3O_4 nanoparticle (φ_{np1}) is held fixed with $\varphi_{np1} = 0.02$. Within the momentum boundary layer, the velocity of $Gr- Fe_3O_4- H_2O$ hybrid nanofluid decreases with φ_{np2} for $U_\infty > U_w$ while the enhancement in φ_{np2} raises the velocity for $U_w > U_\infty$. It is also observed (Fig. 12a and b) that the temperature of hybrid nanofluid flow and thickness of the associated boundary layer are enhanced by increasing φ_{np2}. The reason behind this argument is that the addition of nanoparticles in nanofluid flow helps improve the thermal conductivity of the hybrid nanofluid.

Fig. 13a and b compare the velocity profiles for $Gr- Fe_3O_4- H_2O$ hybrid nanofluid flow ($\varphi_{np1} = 0.1$, $\varphi_{np2} = 0.1$), $Fe_3O_4 - H_2O$ single nanofluid flow ($\varphi_{np1} = 0.2$, $\varphi_{np2} = 0$) and H_2O pure fluid flow ($\varphi_{np1} = 0$, $\varphi_{np2} = 0$). It is concluded that for $U_\infty > U_w$ the velocity field is higher for pure water followed by single nanofluid and hybrid nanofluid flow but opposite behavior is observed for $U_w > U_\infty$. As a result, the hybrid nanofluid has a higher kinematic viscosity leading to thicker velocity boundary layer thickness. Moreover, it is seen (Fig. 14a and b) that the values of temperature for hybrid nanofluid flow are greater than the values of single nanofluid flow and pure fluid flow for both $U_\infty > U_w$ and $U_w > U_\infty$. The reason for this is that compared with magnetite nanoparticles and pure water, graphene nanoparticles have a greater thermal conductivity. Thus, changing the working fluid from H_2O or $Fe_3O_4- H_2O$ to $Gr - Fe_3O_4 - H_2O$ hybrid nanofluid improved the thermal properties, and the temperature rises.

The variation of the non-dimensional temperature with the Eckert number is depicted in Fig. 15. The Eckert number is a parameter to show the effects of viscous dissipation. Physically, the increment in Eckert number leads to friction in the flow field, and as a result, the temperature increases.

Fig. 16 depicts the impact of the space-fractional parameter β on the temperature distribution. Here, $0 < \beta < 1$ corresponds to the fractional diffusion, and for $\beta = 1$, the problem reduces to the case of classical diffusion. It is interesting to note that the space-fractional parameter

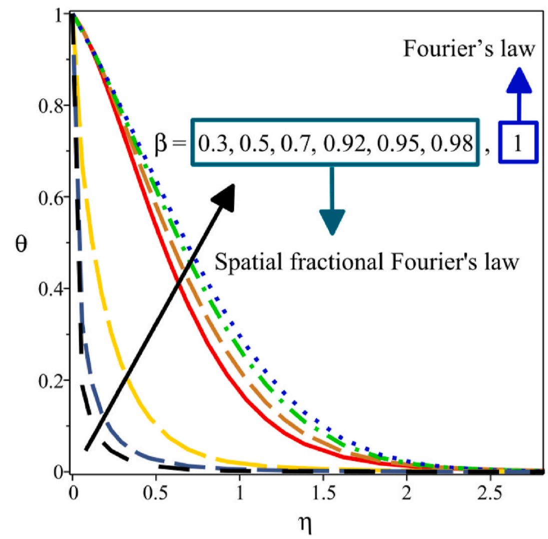

Fig. 16. Temperature profiles for various values of β

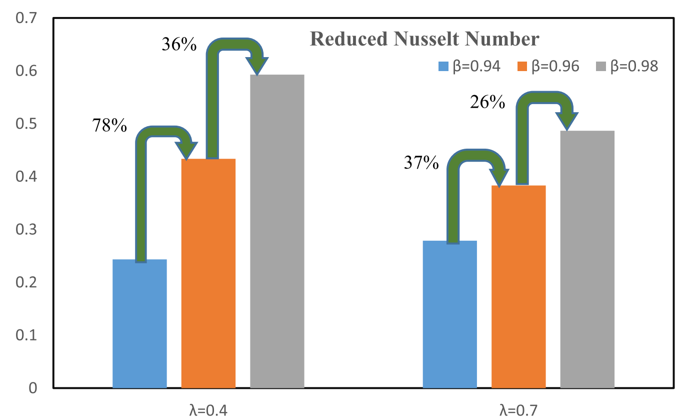

Fig. 17. Comparison of the reduced nusselt number for various values of β

models the nonlocal interaction between the heat flux and the temperature gradient. It turns out (Fig. 16) that the thickness of the thermal boundary layer is thinner for fractional diffusion as compared to classical diffusion. Thus, temperature increases for the larger fractional parameter β. Consequently, it can be concluded that temperature in the spatial fractional Fourier's law model is less than the Fourier's law without the spatial fractional derivative. The influence of the space-fractional parameter (β) on the reduced Nusselt number is shown in Fig. 17. The magnitude of the Nusselt number is augmented via larger space-fractional parameter. Besides, the Nusselt number of the hybrid nanofluid flow is enhanced by 114% for $U_\infty > U_w$ and 63% for $U_w > U_\infty$ at $\beta = 0.98$ when compared with $\beta = 0.94$. The magnitude of the reduced skin friction coefficient and reduced Nusselt number of hybrid nanofluid flow are compared with the single nanofluid and pure water flow in Fig. 18a and b respectively. It is found that the skin friction coefficient for the pure water ($\varphi_{np1} = 0$, $\varphi_{np2} = 0$) is smaller than that for the nanofluid ($\varphi_{np1} = 0.2$, $\varphi_{np2} = 0$) and hybrid nanofluid ($\varphi_{np1} = 0.1$, $\varphi_{np2} = 0.1$). Further, the minimum Nusselt number is noticed for pure water and the maximum Nusselt number is observed for hybrid nanofluid. The results also show that by using the nanofluid and hybrid nanofluid, the Nusselt number is augmented by a value of 75% and 88% for the case $\lambda = 0.4$ and 46% and 68% for the case $\lambda = 0.7$respectively.

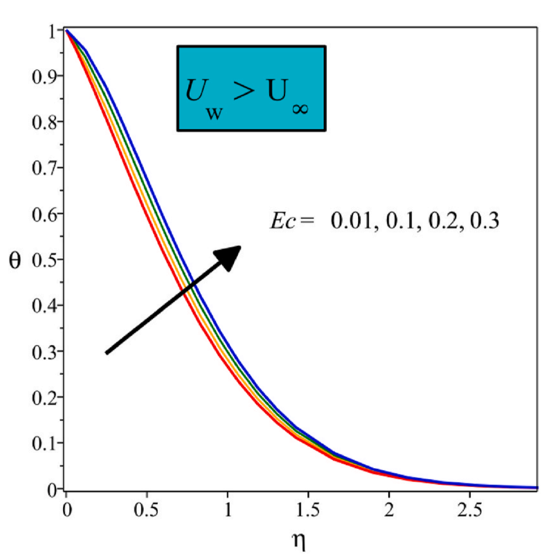

Fig. 15. Temperature profiles for various values of Ec

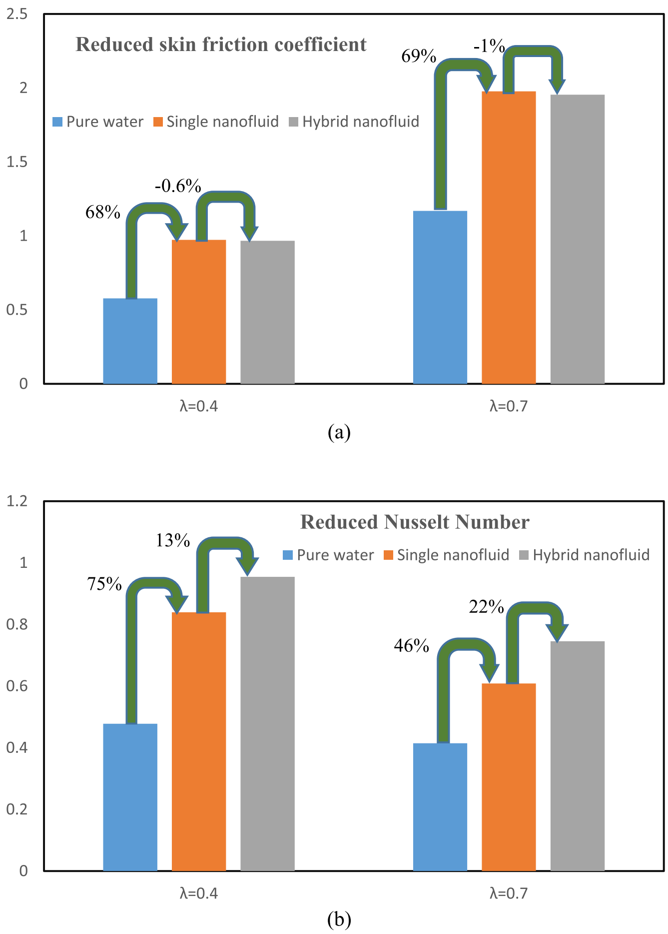

Fig. 18. Comparison of the (a) reduced skin friction coefficient (b) reduced nusselt number for different fluids.

6. Conclusions

In the current study, the hybrid nanofluid boundary layer flow and heat transport of graphene-magnetite-water past a moving flat plate under the impact of MHD are analyzed semi-analytically. The spatial fractional derivatives (the Caputo's derivative operator) are incorporated into Fourier's law. Then, the modified Fourier's law is taken into account in the diffusion term of the energy equation. The key findings can be summarized as follows:

- The hybrid nanofluid flow elevates temperature and corresponding boundary layer thickness more when compared to single and pure fluid flows.
- In the special case of $U_\infty > U_w$, temperature varies as a decreasing function of the Hartmann number and velocity nanofluid ratio parameter.
- The higher space-fractional parameter causes a thicker thermal boundary layer thickness.
- The temperature elevates as the nanoparticle volume fraction increases for both $U_\infty > U_w$ and $U_w > U_\infty$.
- The validations of Nusselt number and Skin friction coefficient for a specific Prandtl number available in the literature are achieved by comparing the results with both the experimental studies and numerical solutions.

Based on the findings of the present investigation we conclude that the OCM may be considered as an efficient semi-analytical method for the spatial-fractional MHD boundary layer flow.

Declaration of competing interest

The authors declare that they have no known competing financial interests or personal relationships that could have appeared to influence the work reported in this paper.

Data availability

No data was used for the research described in the article.

References

[1] B. West, M. Bologna, P. Grigolini, Physics of Fractal Operators, 2003, p. 354, 2003, https://books.google.fr/books/about/Physics_of_Fractal_Operators.html?id=EgyTpQZOga0C&pgis=1.
[2] E.A. Gonzalez, I. Petráš, Advances in fractional calculus: control and signal processing applications, in: Proc. 2015 16th Int. Carpathian Control Conf. ICCC 2015, 2015, pp. 147–152, https://doi.org/10.1109/CarpathianCC.2015.7145064.
[3] H.G. Sun, Y. Zhang, D. Baleanu, W. Chen, Y.Q. Chen, A new collection of real world applications of fractional calculus in science and engineering, Commun. Nonlinear Sci. Numer. Simulat. 64 (2018) 213–231, https://doi.org/10.1016/j.cnsns.2018.04.019.
[4] M. Pan, L. Zheng, C. Liu, F. Liu, P. Lin, G. Chen, A stochastic model for thermal transport of nanofluid in porous media: derivation and applications, Comput, Math. with Appl. 75 (2018) 1226–1236, https://doi.org/10.1016/j.camwa.2017.10.022.
[5] X. Chen, Y. Ye, X. Zhang, L. Zheng, Lie-group similarity solution and analysis for fractional viscoelastic MHD fluid over a stretching sheet, Comput. Math. Appl. 75 (2018) 3002–3011, https://doi.org/10.1016/j.camwa.2018.01.028.
[6] A. Tassaddiq, MHD flow of a fractional second grade fluid over an inclined heated plate, Chaos, Solit. Fractals 123 (2019) 341–346, https://doi.org/10.1016/j.chaos.2019.04.029.
[7] B. Li, F. Liu, Boundary layer flows of viscoelastic fluids over a non-uniform permeable surface, Comput. Math. Appl. 79 (2020) 2376–2387, https://doi.org/10.1016/j.camwa.2019.11.003.
[8] A. Moghadassi, E. Ghomi, F. Parvizian, A numerical study of water based Al2O3 and Al2O3-Cu hybrid nanofluid effect on forced convective heat transfer, Int. J. Therm. Sci. 92 (2015) 50–57, https://doi.org/10.1016/j.ijthermalsci.2015.01.025.
[9] M. Alizadeh, K. Hosseinzadeh, D.D. Ganji, Investigating the effects of hybrid nanoparticles on solid-liquid phase change process in a Y-shaped fin-assisted LHTESS by means of FEM, J. Mol. Liq. 287 (2019) 110931, https://doi.org/10.1016/j.molliq.2019.110931.
[10] A.I. Alsabery, T. Tayebi, H.T. Kadhim, M. Ghalambaz, I. Hashim, A.J. Chamkha, Impact of two-phase hybrid nanofluid approach on mixed convection inside wavy lid-driven cavity having localized solid block, J. Adv. Res. (2020), https://doi.org/10.1016/j.jare.2020.09.008.
[11] H. Maddah, R. Aghayari, M. Mirzaee, M.H. Ahmadi, M. Sadeghzadeh, A. J. Chamkha, Factorial experimental design for the thermal performance of a double pipe heat exchanger using Al2O3-TiO2 hybrid nanofluid, Int. Commun. Heat Mass Tran. 97 (2018) 92–102, https://doi.org/10.1016/j.icheatmasstransfer.2018.07.002.
[12] F. Mabood, G.P. Ashwinkumar, N. Sandeep, Simultaneous results for unsteady flow of MHD hybrid nanoliquid above a flat/slendering surface, J. Therm. Anal. Calorim. (2020), https://doi.org/10.1007/s10973-020-09943-x.
[13] I. Tlili, H.A. Nabwey, S.P. Samrat, N. Sandeep, 3D MHD nonlinear radiative flow of CuO-MgO/methanol hybrid nanofluid beyond an irregular dimension surface with slip effect, Sci. Rep. 10 (2020), https://doi.org/10.1038/s41598-020-66102-w.
[14] S. Askari, H. Koolivand, M. Pourkhalil, R. Lotfi, A. Rashidi, Investigation of Fe3O4/Graphene nanohybrid heat transfer properties: experimental approach, Int. Commun. Heat Mass Tran. 87 (2017) 30–39, https://doi.org/10.1016/j.icheatmasstransfer.2017.06.012.
[15] F. Mabood, G.P. Ashwinkumar, N. Sandeep, Effect of nonlinear radiation on 3D unsteady MHD stagnancy flow of Fe3O4/graphene–water hybrid nanofluid, Int. J. Ambient Energy (2020), https://doi.org/10.1080/01430750.2020.1831593.
[16] P. Tao, L. Shu, J. Zhang, C. Lee, Q. Ye, H. Guo, T. Deng, Silicone oil-based solar-thermal fluids dispersed with PDMS-modified Fe3O4@graphene hybrid nanoparticles, Prog. Nat. Sci. Mater. Int. 28 (2018) 554–562, https://doi.org/10.1016/j.pnsc.2018.09.003.
[17] H. Sardar, L. Ahmad, M. Khan, A.S. Alshomrani, Investigation of mixed convection flow of Carreau nanofluid over a wedge in the presence of Soret and Dufour effects, Int. J. Heat Mass Tran. 137 (2019) 809–822, https://doi.org/10.1016/j.ijheatmasstransfer.2019.03.132.
[18] O.D. Makinde, W.A. Khan, Z.H. Khan, Stagnation point flow of MHD chemically reacting nanofluid over a stretching convective surface with slip and radiative heat, in: Proc. Inst. Mech. Eng. Part E J. Process Mech. Eng., vol. 231, 2017, pp. 695–703, https://doi.org/10.1177/0954408916629506.
[19] H.M. Elshehabey, Z. Raizah, H.F. Öztop, S.E. Ahmed, MHD natural convective flow of Fe3O4−H2O ferrofluids in an inclined partial open complex-wavy-walls ringed enclosures using non-linear Boussinesq approximation, Int. J. Mech. Sci. 170 (2020), https://doi.org/10.1016/j.ijmecsci.2019.105352.
[20] D. Sáchica, C. Treviño, L. Martínez-Suástegui, Numerical study of magnetohydrodynamic mixed convection and entropy generation of Al2O3-water

nanofluid in a channel with two facing cavities with discrete heating, Int. J. Heat Fluid Flow 86 (2020), https://doi.org/10.1016/j.ijheatfluidflow.2020.108713.
[21] S. Nadeem, R. Mehmood, S.S. Motsa, Numerical investigation on MHD oblique flow of Walter's B type nano fluid over a convective surface, Int. J. Therm. Sci. 92 (2015) 162–172, https://doi.org/10.1016/j.ijthermalsci.2015.01.034.
[22] W. Ibrahim, O.D. Makinde, Magnetohydrodynamic stagnation point flow and heat transfer of casson nanofluid past a stretching sheet with slip and convective boundary condition, J. Aero. Eng. 29 (2016), 04015037, https://doi.org/10.1061/(asce)as.1943-5525.0000529.
[23] T. Hayat, T. Muhammad, S.A. Shehzad, A. Alsaedi, An analytical solution for magnetohydrodynamic Oldroyd-B nanofluid flow induced by a stretching sheet with heat generation/absorption, Int. J. Therm. Sci. 111 (2017) 274–288, https://doi.org/10.1016/j.ijthermalsci.2016.08.009.
[24] K.U. Rehman, A.A. Khan, M.Y. Malik, O.D. Makinde, Thermophysical aspects of stagnation point magnetonanofluid flow yields by an inclined stretching cylindrical surface: a non-Newtonian fluid model, J. Brazilian Soc. Mech. Sci. Eng. 39 (2017) 3669–3682, https://doi.org/10.1007/s40430-017-0860-3.
[25] C. Sulochana, S.P. Samrat, N. Sandeep, Boundary layer analysis of an incessant moving needle in MHD radiative nanofluid with joule heating, Int. J. Mech. Sci. 128–129 (2017) 326–331, https://doi.org/10.1016/j.ijmecsci.2017.05.006.
[26] C.J. Huang, Influence of non-Darcy and MHD on free convection of non-Newtonian fluids over a vertical permeable plate in a porous medium with soret/dufour effects and thermal radiation, Int. J. Therm. Sci. 130 (2018) 256–263, https://doi.org/10.1016/j.ijthermalsci.2018.04.019.
[27] B. Souayeh, M.G. Reddy, P. Sreenivasulu, T. Poornima, M. Rahimi-Gorji, I. M. Alarifi, Comparative analysis on non-linear radiative heat transfer on MHD Casson nanofluid past a thin needle, J. Mol. Liq. 284 (2019) 163–174, https://doi.org/10.1016/j.molliq.2019.03.151.
[28] M. Veera Krishna, Hall and ion slip impacts on unsteady MHD free convective rotating flow of Jeffreys fluid with ramped wall temperature, Int. Commun. Heat Mass Tran. 119 (2020), https://doi.org/10.1016/j.icheatmasstransfer.2020.104927.
[29] M. Azam, A. Shakoor, H.F. Rasool, M. Khan, Numerical simulation for solar energy aspects on unsteady convective flow of MHD Cross nanofluid: a revised approach, Int. J. Heat Mass Tran. 131 (2019), https://doi.org/10.1016/j.ijheatmasstransfer.2018.11.022.
[30] S.P. Samrat, M.G. Reddy, N. Sandeep, Buoyancy effect on magnetohydrodynamic radiative flow of Casson fluid with Brownian moment and thermophoresis, Eur. Phys. J. Spec. Top. 230 (2021) 1273–1281, https://doi.org/10.1140/epjs/s11734-021-00043-x.
[31] L. Beghin, M. Caputo, Commun Nonlinear Sci Numer Simulat Commutative and associative properties of the Caputo fractional derivative and its generalizing convolution operator, Commun. Nonlinear Sci. Numer. Simulat. 89 (2020) 105338, https://doi.org/10.1016/j.cnsns.2020.105338.
[32] S. Mukhopadhyay, K. Bhattacharyya, G.C. Layek, Steady boundary layer flow and heat transfer over a porous moving plate in presence of thermal radiation, Int. J. Heat Mass Tran. 54 (2011) 2751–2757, https://doi.org/10.1016/j.ijheatmasstransfer.2011.03.017.
[33] M. Pan, L. Zheng, F. Liu, X. Zhang, Modeling heat transport in nanofluids with stagnation point flow using fractional calculus, Appl. Math. Model. 40 (2016) 8974–8984, https://doi.org/10.1016/j.apm.2016.05.044.
[34] M. Khazayinejad, M. Hatami, D. Jing, M. Khaki, G. Domairry, Boundary layer flow analysis of a nanofluid past a porous moving semi-infinite flat plate by optimal collocation method, Powder Technol. 301 (2016) 34–43, https://doi.org/10.1016/j.powtec.2016.05.053.
[35] S.S. Ghadikolaei, M. Gholinia, M.E. Hoseini, D.D. Ganji, Natural convection MHD flow due to MoS 2 –Ag nanoparticles suspended in C 2 H 6 O 2 [sbnd]H 2 O hybrid base fluid with thermal radiation, J. Taiwan Inst. Chem. Eng. 97 (2019) 12–23, https://doi.org/10.1016/j.jtice.2019.01.028.
[36] N. Acharya, R. Bag, P.K. Kundu, On the impact of nonlinear thermal radiation on magnetized hybrid condensed nanofluid flow over a permeable texture, Appl. Nanosci. 10 (2020) 1679–1691, https://doi.org/10.1007/s13204-019-01224-w.
[37] M. Hatami, Cross-sectional heat transfer of hot tubes in a wavy porous channel filled by Fe3O4-water nanofluid under a variable magnetic field, Eur. Phys. J. Plus. 133 (2018), https://doi.org/10.1140/epjp/i2018-12170-3.
[38] E.H. Aly, Dual exact solutions of graphene–water nanofluid flow over stretching/shrinking sheet with suction/injection and heat source/sink: critical values and regions with stability, Powder Technol. 342 (2019) 528–544, https://doi.org/10.1016/j.powtec.2018.09.093.
[39] F.P. Incropera, Fundamentals of Heat and Mass Transfer, sixth ed., John Wiley & Sons, United States, 2006, pp. 1689–1699. J. Chem. Inf. Model. 53 (2013).
[40] M. Hatami, M. Khazayinejad, D. Jing, Forced convection of Al2O3–water nanofluid flow over a porous plate under the variable magnetic field effect, Int. J. Heat Mass Tran. 102 (2016) 622–630, https://doi.org/10.1016/j.ijheatmasstransfer.2016.06.075.
[41] S.S. Nourazar, M. Hatami, D.D. Ganji, M. Khazayinejad, Thermal-flow boundary layer analysis of nanofluid over a porous stretching cylinder under the magnetic field effect, Powder Technol. 317 (2017) 310–319, https://doi.org/10.1016/j.powtec.2017.05.010.
[42] M. Hatami, A. Hasanpour, D.D. Ganji, Heat transfer study through porous fins (Si 3 N 4 and AL) with temperature-dependent heat generation, Energy Convers. Manag. 74 (2013) 9–16, https://doi.org/10.1016/j.enconman.2013.04.034.
[43] A.S. Mohammadein, M.F. El-Amin, H.M. Ali, An approximate similarity solution for spatial fractional boundary-layer flow over an infinite vertical plate, Comput. Appl. Math. 39 (2020), https://doi.org/10.1007/s40314-020-01144-4.
[44] M. Hatami, D.D. Ganji, Heat transfer and nanofluid flow in suction and blowing process between parallel disks in presence of variable magnetic field, J. Mol. Liq. 190 (2014) 159–168, https://doi.org/10.1016/j.molliq.2013.11.005.
[45] S. Dhawan, Direct Measurements of Skin Friction, 1953. NACA-TR-1121, https://ntrs.nasa.gov/citations/19930092157.
[46] G.H. Junkhan, G.K. Serovy, Effects of free-stream turbulence and pressure gradient on flat-plate boundary-layer velocity profiles and on heat transfer, J. Heat Tran. 89 (1967) 169–175, https://doi.org/10.1115/1.3614346.
[47] H. Schlichting, K. Gersten, Boundary-Layer Theory, 2016, https://doi.org/10.1007/978-3-662-52919-5.
[48] B.C. Sakiadis, Boundary-layer behavior on continuous solid surfaces: II. The boundary layer on a continuous flat surface, AIChE J. 7 (1961) 221–225, https://doi.org/10.1002/aic.690070211.
[49] H. Blasius, Grenzschichten in Flussigkeiten mit kleiner Reibung, Z. Math. Phys. 56 (1908) 1–37.
[50] J.A. Schetz, R.D.W. Bowersox, Boundary Layer Analysis, second ed., 2011, https://doi.org/10.2514/4.868245.
[51] A. Ishak, R. Nazar, I. Pop, Boundary-layer flow of a micropolar fluid on a continuously moving or fixed permeable surface, Int. J. Heat Mass Tran. 50 (2007) 4743–4748, https://doi.org/10.1016/j.ijheatmasstransfer.2007.03.034.
[52] E. Pohlhausen, Der Wärmeaustausch zwischen festen Körpern und Flüssigkeiten mit kleiner reibung und kleiner Wärmeleitung, ZAMM - J. Appl. Math. Mech./Z. Angew. Math. Mech. 1 (1921) 115–121, https://doi.org/10.1002/zamm.19210010205.
[53] P.H. Oosthuizen, D. Naylor, An Introduction to Convective Heat Transfer Analysis, 1999.
[54] C.H. Chen, Forced convection over a continuous sheet with suction or injection moving in a flowing fluid, Acta Mech. 138 (1999) 1–11, https://doi.org/10.1007/BF01179537.
[55] N. Bachok, A. Ishak, I. Pop, Boundary layer flow and heat transfer with variable fluid properties on a moving flat plate in a parallel free stream, J. Appl. Math. 2012 (2012), https://doi.org/10.1155/2012/372623.